PHYSICAL REVIEW A **81**, 063418 (2010)

Ionization of oriented targets by intense circularly polarized laser pulses: Imprints of orbital angular nodes in the two-dimensional momentum distribution

C. P. J. Martiny, M. Abu-samha, and L. B. Madsen
Lundbeck Foundation Theoretical Center for Quantum System Research,
Department of Physics and Astronomy, Aarhus University, DK-8000 Aarhus C, Denmark

(Received 8 April 2010; published 21 June 2010)

We solve the three-dimensional time-dependent Schrödinger equation for a few-cycle circularly polarized femtosecond laser pulse that interacts with an oriented target exemplified by an argon atom, initially in a $3p_x$ or $3p_y$ state. The photoelectron momentum distributions show distinct signatures of the orbital structure of the initial state as well as the carrier-envelope phase of the applied pulse. Our *ab initio* results are compared with results obtained using the length-gauge strong-field approximation, which allows for a clear interpretation of the results in terms of classical physics. Furthermore, we show that ionization by a circularly polarized pulse completely maps out the angular nodal structure of the initial state, thus providing a potential tool for studying orbital symmetry in individual systems or during chemical reactions.

DOI: 10.1103/PhysRevA.81.063418 PACS number(s): 32.80.Rm

I. INTRODUCTION

The recent decades have shown substantial progress in strong-field physics with pulsed lasers. Pulses with field strengths equivalent to the field of the Coulomb interaction in ground-state atoms and durations of only a few femtoseconds are now available for a large range of wavelengths [1,2]. This development has facilitated the opening of exciting research areas, such as attoscience [1,2], which, in turn, has set entirely new standards for the interrogation of atomic and molecular dynamics. Strong-field ionization is a process of special relevance and importance within strong-field physics, since ionization triggers other strong-field phenomena, such as high-order harmonic generation, the key process for generating coherent attosecond pulses in the XUV regime. In strong-field studies there is also an interest in creating unique quantum targets by molecular alignment and orientation techniques [3]. Spatial control of molecules is of importance within attoscience, femtochemistry, and molecular reactivity among others. Recent experiments not only succeeded in alignment of molecules but also in three-dimensional (3D) orientation, thus giving complete control over the spatial orientation [4–9].

The development described here motivates a detailed investigation of ionization of oriented targets by strong laser pulses with special emphasis on orbital structure (e.g., effects of orbital symmetry). The bulk of experimental and theoretical works within strong-field physics have dealt with linearly polarized laser pulses, and there is now a growing interest in the study of ionization of atoms and molecules by elliptically polarized pulses [10–14]. The effects of angular orbital structure in the ionization by linearly polarized fields have previously been studied for direct electrons [15,16] as well as for rescattered electrons [17,18]. When it comes to the probing of angular orbital structure through photoelectron angular distributions or momentum distributions, the use of a strong circularly polarized probe rather than a linearly polarized one has, however, two major advantages: (i) In the circularly polarized field, an electron born in the continuum is constantly driven away from the nucleus, owing to the polarization. This dynamics minimizes rescattering effects as well as interference between wave packets launched at different instants of time during the driving pulse. Thus, the use of circularly polarized laser pulses entails a cleaner ionization signal with respect to orbital structure. (ii) The polarization plane is two dimensional, which permits for a more transparent interrogation of angular orbital structure as we shall see in the present work. In fact, it has recently been shown experimentally that strong-field ionization of 3D-oriented C_7H_5N molecules by a circularly polarized field polarized in the nodal planes of the outermost orbitals provides a unique probe of the angular nodal structure [19].

In this paper we focus on the case where the laser polarization plane is perpendicular to the nodal plane. We calculate, by solving the time-dependent Schrödinger equation (TDSE), the photoelectron momentum distribution for ionization of an argon atom initially prepared in a $3p_x$ or $3p_y$ state modeling an oriented target with a single nodal plane. The $3p_x$ and $3p_y$ states, in particular, serve as models for investigating ionization of a molecular orbital with π symmetry. In the strong near-infrared laser field, the ionization is tunnelinglike and the photoelectron is born in the continuum at a relatively large distance from the center of mass. After the ionization, the circularly polarized field drives the electron away from the core, which in turn minimizes the importance of the detailed structure of the molecular potential at small distances. The calculations are compared with results obtained using the length gauge strong-field approximation (LG-SFA) [20–22], which facilitates interpretation using semiclassical theory [23]. Our results show distinct effects of the angular nodal structure of the initial orbital. For example, the angular nodal structure of p_x, p_y and d_{xy} orbitals is readily mapped out, showing that strong-field ionization by a circularly polarized laser pulse directly probes the nodal structure. These are rather simple systems, so in order to further stress the potential of the method, we show that the angular nodal structure of a benzene molecule is mapped uniquely to the momentum distribution.

This paper is organized as follows. In Sec. II we briefly review the basic theory behind the computations. In Sec. III we discuss the results and in Sec. IV we give our conclusions. Atomic units [$\hbar = a_0 = m_e = 1$] are used throughout, unless stated otherwise.

II. THEORY

We investigate an oriented target, modeled by an Ar atom initially prepared in a $3p_x$ or $3p_y$ state, interacting with a circularly polarized few-cycle pulse also in the xy plane. The electric field is defined as $\vec{E} = -\partial_t \vec{A}$ with the vector potential $\vec{A}(t)$,

$$\vec{A}(t) = \frac{A_0}{\sqrt{2}} f(t) \begin{pmatrix} \cos(\omega_0 t + \phi) \\ \sin(\omega_0 t + \phi) \\ 0 \end{pmatrix}. \tag{1}$$

Here A_0 denotes the amplitude, ω_0 the carrier frequency, ϕ the carrier-envelope phase (CEP), and $f(t) = \sin^2(\frac{\omega_0 t}{2N})$ the envelope, with N the number of optical cycles. The laser field couples primarily to the least bound electron, which in turn motivates the use of the single-active electron approximation (SAE). Hence, our analysis is restricted to the outermost electron, the remaining being described by an effective potential [24]. The photoelectron momentum distribution is given by

$$\frac{\partial^3 P}{\partial q_x \partial q_y \partial q_z} = |\langle \Psi_{\vec{q}}^{-}(\vec{r}) | \Psi(\vec{r},T)\rangle|^2, \tag{2}$$

where $\Psi_{\vec{q}}^{-}(\vec{r})$ is a continuum scattering wave function of asymptotic momentum $\vec{q}$ and $\Psi(\vec{r},T)$ is the wave packet at the end of the pulse T. We calculate the wave packet by expanding in a spherical harmonic basis for the angular part and reduced radial wave functions $f_{lm}(r,t)$ defined on a radial grid, $\Psi(\vec{r},t) = \sum_{l=0}^{l_{\max}} \sum_{m=-l}^{l} (f_{lm}(r,t)/r) Y_{lm}(\theta,\phi)$, and then solving the TDSE in the velocity gauge using a split-step method. The details are described elsewhere [25,26]. The scattering states entering in Eq. (2) are obtained by solving the time-independent Schrödinger equation for the effective potential.

The LG-SFA [20,21], which completely neglects the Coulomb interaction in the final state as well as all intermediate states, offers a simple formula for the momentum distribution,

$$\frac{\partial^3 P}{\partial q_x \partial q_y \partial q_z} = \left| \int_0^T \langle \Psi_{\vec{q}}^{V}(\vec{r},t) | \vec{E} \cdot \vec{r} | \Psi_i(\vec{r},t)\rangle dt \right|^2, \tag{3}$$

where $\Psi_{\vec{q}}^{V}$ is a Volkov wave function with asymptotic momentum $\vec{q}$ and Ψ_i is the initial state. In the evaluation of Eq. (3) it is accurate to use the asymptotic form of the initial state, $\Psi_i(\vec{r},t) = \sum_{lm} C_{lm} r^{\nu-1} \exp(-\kappa r) Y_{lm}(\theta,\phi) \exp(i I_p t)$, since ionization primarily occurs at large distances from the nucleus. Here I_p denotes the ionization potential, $\kappa = \sqrt{2 I_p}$, and $\nu = Z/\kappa$ with Z the charge of the residual ion. The spatial integration in Eq. (3) can be performed analytically within this approximation, while the one-dimensional (1D) time integral is evaluated effectively using the saddle-point approximation [27], which is accurate in the parameter regime considered in this paper [28,29].

III. RESULTS

A. Imprints of nodal planes in momentum distributions

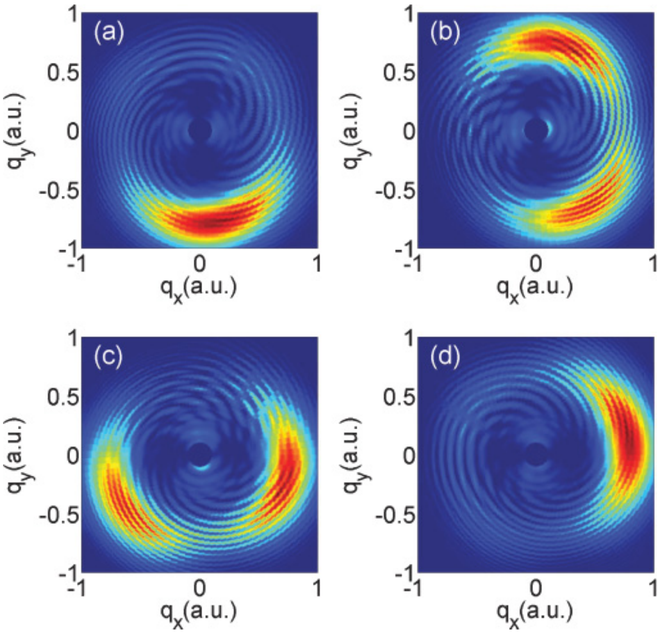

FIG. 1. (Color online) Momentum distributions from the single-active-electron TDSE calculation for the [(a) and (b)] $3p_x$ and [(c) and (d)] $3p_y$ states of Ar in the xy polarization plane for the following choice of laser parameters: angular frequency $\omega = 0.057$, corresponding to 800 nm, peak intensity $I = 1.06 \times 10^{14}$ W/cm^2, carrier-envelope phase [(a) and (c)] $\varphi = -\pi/2$, [(b) and (d)] $\varphi = 0$, and number of optical cycles $N = 3$.

Figure 1 shows the TDSE results for the momentum distributions in the xy plane of polarization for the $3p_x$ [1(a) and 1(b)] and $3p_y$ [1(c) and 1(d)] initial states of Ar, probed by an 800-nm three-cycle laser pulse with peak intensity $I = 1.06 \times 10^{14}$ W/cm^2 and CEP $\varphi = -\pi/2$ [1(a) and 1(c)] and $\varphi = 0$ [1(b) and 1(d)]. The distributions are calculated using a 4096-points radial grid extending to $r_{\max} = 400$, maximum angular momentum $l_{\max} = 40$, and a time step of 0.005. Notice that the ionization potential for the Ar($3p$) state is 15.76 eV. The low-energy part $\sqrt{q_x^2 + q_y^2} < 0.1$ has been removed for better graphical display. For the $3p_x$ state with $\phi = -\pi/2$ [Fig. 1(a)] and $3p_y$ state with $\phi = 0$ [Fig. 1(d)], we observe a distribution with a single dominant peak, which, as we shall discuss in more detail below, is located near $\vec{q} \approx -\vec{A}(T/2)$. In the two other cases we observe a splitting of this peak into two nearly symmetric peaks. As we now show these main features are explained using the LG-SFA. Figure 2 shows the momentum distributions obtained by using the LG-SFA in the plane of polarization for the $3p_x$ [2(a) and 2(b)] and $3p_y$ [2(c) and 2(d)] initial states of Ar, at 800-nm light and peak intensity $I = 1.06 \times 10^{14}$ W/cm^2, CEP $\varphi = -\pi/2$ [2(a) and 2(c)], $\varphi = 0$ [2(b) and 2(d)], and three optical cycles $N = 3$.

The SFA results clearly reproduce the general structures of the TDSE distributions, except for an overall angular shift and a spiral-like interference structure. The former overall angular shift is due partly to the Columbic interaction, and partly to the fact that the laser field breaks the rotational invariance perpendicular to the polarization plane [14]. This feature has been observed experimentally in the ionization of helium by a few-cycle circularly polarized laser pulse [11]. The spiral structure is connected to the interaction between outgoing

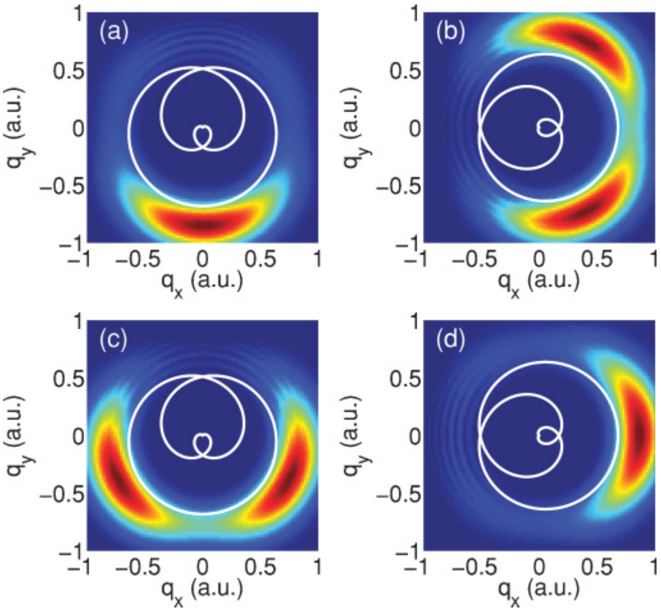

FIG. 2. (Color online) SFA momentum distributions for the [(a) and (b)] $3p_x$ and [(c) and (d)] $3p_y$ states of Ar in the xy polarization plane for the following choice of laser parameters: angular frequency $\omega = 0.057$, corresponding to 800 nm, peak intensity $I = 1.06 \times 10^{14}$ W/cm^2, CEP $\varphi = -\pi/2$ [(a) and (c)], $\varphi = 0$ [(b) and (d)], and a number of optical cycles $N = 3$. The white curves show a parametric plot of $-\vec{A}(t)$ from Eq. (1). If no nodal planes are along the polarization at time $t = T/2$, the dominating peak in the distribution follows the simple formula $\vec{q}_{\text{final}} \simeq -\vec{A}(T/2)$ as seen in (a) and (d). If, on the other hand, the field peaks in the direction of the angular node (b), (c) then the dominating peak in the distribution, splits simply because there is no charge density in that direction.

low-energy electrons and the long-range Coulomb potential, equivalent to the radial fans seen in the linear case [30–34].

It is well known, in the case of a spherically symmetric initial state, that the LG-SFA momentum distribution reflects the shape of the vector potential [28]. This is easily explained by semiclassical theory [23]: Owing to the exponential dependence of the rate on the field strength, ionization predominantly occurs at the times t when the magnitude of the electric field is close to the maximum $|\vec{E}(T/2)|$. Assuming that the (classical) electron is born in the continuum with zero initial velocity and that it subsequently moves under the influence of the electric field only, we obtain $\vec{q}_{\text{final}} = -\vec{A}(t_i)$ with t_i the instant of ionization [$\vec{q}_{\text{final}} = -\vec{A}(T/2)$ dominates]. However, in the case of a nonspherical initial state, this simple argument has to be extended to take into account the shape of the initial state, in particular the angular nodal structure. For example, it may happen that the field is in a nodal plane of the initial state at $t = T/2$ and hence ionization will be suppressed. In other words, in this more general case, the shape of the vector potential, electric field, and initial state, that determine the overall structure of the momentum distribution. The results in Figs. 1 and 2 clearly illustrate this combined effect. Let us start by analyzing the results for the $3p_x$ state and let us concentrate on the LG-SFA results to make the discussion as simple as possible. Figure 2(a) shows the SFA momentum distribution in the plane of polarization for $\phi = -\pi/2$ and the $3p_x$ initial state. We observe a distribution with a single peak located near $-\vec{A}(T/2)$, in good agreement with the semiclassical theory. In the case of $\varphi = -\pi/2$, $\vec{E}(T/2) = E_x(T/2)\hat{x}$ points in the direction of maximum electron density [see Fig. 3(a)], while both $\vec{E}$ and $3p_x$ are symmetric with respect to $(x,y) \rightarrow (x,-y)$. This leads to a single peak situated at $\vec{q} \sim -\vec{A}(T/2) \propto -\hat{y}$ and symmetric with respect to $(q_x,q_y) \rightarrow (-q_x,q_y)$ in good agreement with the calculated distribution. Figure 2(b) shows the SFA momentum distribution, in the plane of polarization, for $\phi = 0$ and a $3p_x$ initial state. We observe two peaks, symmetric with respect to $(q_x,q_y) \rightarrow (q_x,-q_y)$, in contrast to the simplest single peak semiclassical prediction. In the case of $\varphi = 0$, $\vec{E}(T/2) = E_y(T/2)\hat{y}$ lies in the nodal plane of $3p_x$ [see Fig. 3(b)], hence we do not have ionization in the direction of field maximum. Thus, the single peak from before splits into two symmetric peaks, owing to the fact that $\vec{E}$ and $3p_x$ are symmetric with respect to $(x,y) \rightarrow (-x,y)$, again in good agreement with the obtained distribution. The precise location of the peaks is determined by a competition between the rate arising from the electric field and the density profile of the initial state. The results shown in Figs. 2(c) and 2(d) are explained using similar reasoning. Notice that the signature of the nodal plane in the momentum distribution is advanced by $\pi/2$ compared to the orbital angular nodal structure, reflecting the $\pi/2$ phase between the electric field and the vector potential.

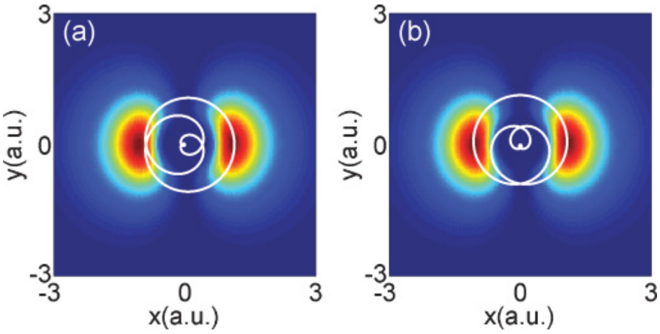

FIG. 3. (Color online) Electron density in the $3p_x$ state of Ar together with a parametric plot of the electric field, corresponding to the vector potential shown in Fig. 2, scaled by a factor. In (a) $\varphi = -\pi/2$, the electric field at the peak of the pulse $t = T/2$ points in a direction where the orbital density is largest. In (b), $\varphi = 0$, the electric field at the peak of the pulse runs through the orbital node (no electron density).

The preceding discussion of Figs. 1, 2, and 3 clearly shows that the nodal structure of the initial orbital is mapped uniquely to the momentum distribution when the laser polarization plane is perpendicular to the nodal plane. This effect is even more visible in the case of a slightly longer femtosecond pulse, where the asymmetry caused by the CEP of the pulse is smaller. Figure 4 shows the following SFA momentum distribution in the plane of polarization $\partial^2 P/\partial q_x \partial q_y = \int (\partial^3 P/\partial q_x \partial q_y \partial q_z) dq_z$ for H($1s$), H($2p_x$), H($2p_y$), and H($3d_{xy}$) states obtained using the same parameters as in Figs. 1 and 2, except that the number of optical cycles was increased to $N = 20$ and $I = 1.0 \times 10^{14}$ W/cm^2. The use of the LG-SFA is for computational convenience and is justified by the results presented on Ar. The binding energy of the

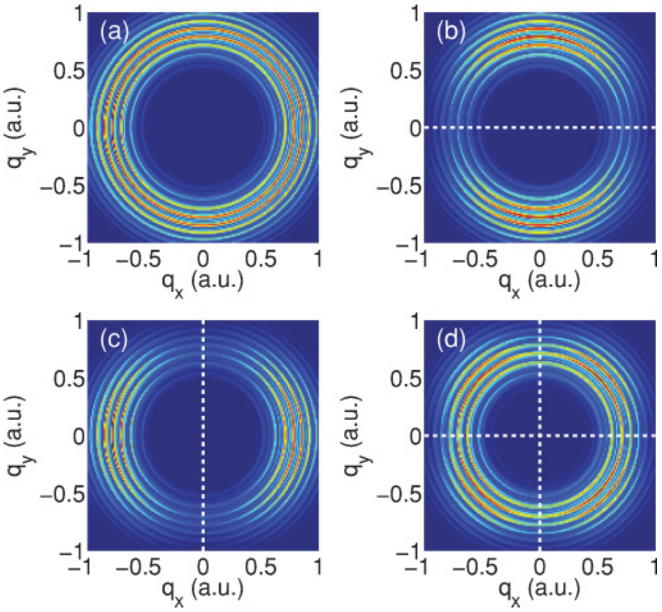

FIG. 4. (Color online) SFA momentum distributions $\partial^2 P/\partial q_x \partial q_y = \int (\partial^3 P/\partial q_x \partial q_y \partial q_z) dq_z$ for (a) $1s$, (b) $2p_x$, (c) $2p_y$, and (d) $3d_{xy}$, obtained using the following laser parameters: angular frequency $\omega = 0.057$, corresponding to 800 nm, peak intensity $I = 1.0 \times 10^{14}$ W/cm^2, carrier-envelope phase $\varphi = 0$, and number of optical cycles $N = 20$. The binding energy of the $2p_x$, $2p_y$, and $3d_{xy}$ states are modified to the ground-state energy of H. The white dashed lines show regions where ionization is suppressed.

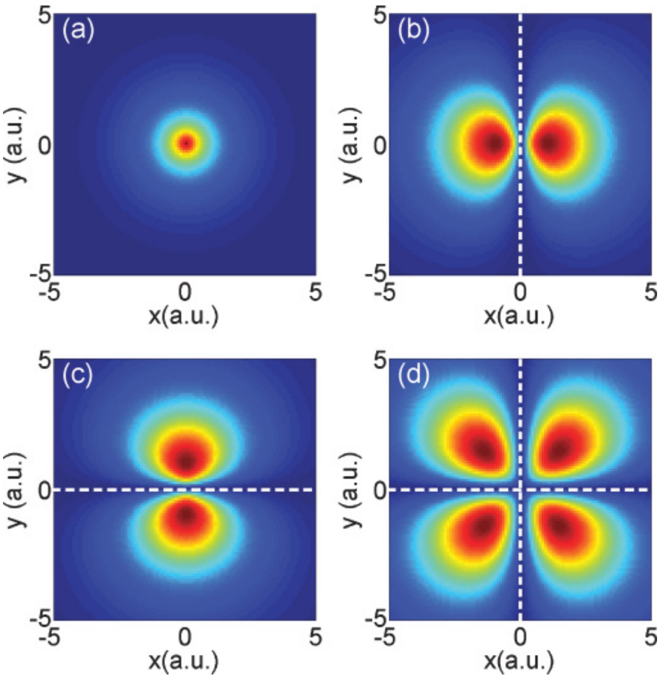

FIG. 5. (Color online) The asymptotic density for (a) H($1s$), (b) H($2p_x$), (c) H($2p_y$), and (d) H($3d_{xy}$). The white dashed lines show the angular nodal planes.

H($2p_x$), H($2p_y$), and H($3d_{xy}$) have been artificially modified to −0.5 (by modifying $\kappa = \sqrt{2I_p}$) in order to compare with the H($1s$) result. Figure 4 clearly shows that the angular nodal structure is mapped uniquely to the momentum distribution. This is particularly clear when compared with Fig. 5, which shows the asymptotic densities for the $1s$, $2p_x$, $2p_y$, and $3d_{xy}$ states. The electric field is almost constant during the dominant cycles of the field (i.e., there is no competition between the rate arising from the electric field and the density profile). In the case of H($1s$) we observe a completely symmetric distribution with well-resolved above-threshold ionization peaks, while ionization is strongly suppressed along the q_x axis (q_y axis) in the case of H($2p_x$) [H($2p_y$)] and along the q_x axis and q_y axis in the case of H($3d_{xy}$), reflecting the angular nodal structures in Fig. 5. Ionization is suppressed along the q_x axis (q_y axis) in the case of H($2p_x$) [H($2p_y$)], owing to the yz (xz) nodal plane which is shifted 90° by the vector potential. There are two angular nodal planes for H($3d_{xy}$), namely the xz and yz planes, suppressing ionization along the y axis and x axis.

Figure 6(a) shows the momentum distribution in the xy plane associated with strong- field ionization of the highest occupied molecular orbital (HOMO) of the benzene molecule [Fig. 6(b)]; the molecule lies in the yz plane. The laser parameters are $\omega = 0.057$, laser peak intensity 5.0×10^{13} W/cm^2, and $N = 10$ optical cycles. The asymptotic coefficients for the HOMO are calculated in the following manner: First the wave function is calculated using standard quantum chemistry codes [35]. Then the asymptotic coefficients are determine by fitting the wave function with the known asymptotic wave function [22]. Benzene has two degenerate HOMO orbitals: The first one (not shown) has a nodal plane coinciding with the xy plane, whereas the second, $(C_{2-1}, C_{21}, C_{4-1}, C_{41}, C_{6-1}, C_{61}) = (0.74, -0.74, -0.27, 0.27, 0.04, -0.04)$ and $I_p = 9.24$ eV [contours in Fig. 6(b)] has a nodal plane coinciding with the xz plane. The first degenerate orbital does not contribute to ionization in the xy plane, from symmetry arguments. The second degenerate orbital has one additional nodal plane in yz, which makes it similar to the $H(3d_{xy})$. However, note that the charge density is not fourfold symmetric, and one node is shallower than the other. All these features are indeed mapped uniquely in the momentum distribution [Fig. 6(a)], which reveal two nodal structures, one of which is more clear

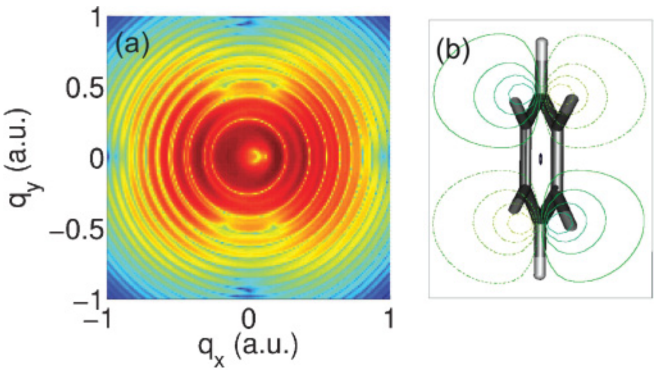

FIG. 6. (Color online) (a) SFA momentum distribution in the xy polarization plane for a benzene molecule oriented in the yz plane. (b) Plot of the participating orbital. The calculation is performed with the following laser parameters: angular frequency $\omega = 0.057$, corresponding to 800 nm, peak intensity $I = 5.0 \times 10^{13}$ W/cm^2, and number of optical cycles $N = 10$.

than the other. The benzene case demonstrates the potential of this method for interrogating the orbital structure of large and complex molecules.

B. Carrier-envelope phase effects in circularly polarized fields

In Figs. 1 and 2, we note that changing the CEP from $\varphi = -\pi/2$ to $\varphi = 0$ does not correspond to a counterclockwise rotation of angle $\pi/2$, contrary to what one might expect: CEP effects for atoms and linear molecules aligned along the propagation axis of the applied circularly polarized field were characterized in terms of simple rotations of the total system around the propagation axis [36]. This characterization, however, only holds when the initial state is invariant with respect to rotations around the propagation direction or when the system initially is described by a uniform incoherent mixture of magnetic substates. The latter point was not discussed explicitly in [36] and we use the opportunity to do so now. Note that CEP effects have been described generally in a Floquet-type approach [37,38].

Consider an atom or a linear molecule, described within the SAE approximation, interacting with a laser pulse described by the vector potential $\vec{A}(t)$ defined in Eq. (1). We assume that the field-free Hamiltonian H_0 is invariant under rotations around the z axis. Furthermore, we assume that the probability for a specific magnetic quantum number P_M is uniform. The ensemble average of $\partial^3 P/\partial q_x \partial q_y \partial q_z$ is defined as [39]

$$\left[\frac{\partial^3 P}{\partial q_x \partial q_y \partial q_z}(\vec{q},\phi)\right] = \mathrm{Tr}\big(\rho(\phi;t)\hat{P}_{\vec{q}}\big), \tag{4}$$

where t is any time after the pulse, $\rho(\phi;t)$ is the density matrix of the total system, ϕ is the CEP, and $\hat{P}_{\vec{q}} = |\Psi_{\vec{q}}^-\rangle\langle\Psi_{\vec{q}}^-|$ projects on the exact scattering states $|\Psi_{\vec{q}}^-\rangle$ with asymptotic momentum $\vec{q}$. The density matrix is given by

$$\rho(\phi;t) = \sum_{M=-J}^{J} P_M |\Psi_{nJM}(\phi;t)\rangle\langle\Psi_{nJM}(\phi;t)|. \tag{5}$$

Here $P_M = \frac{1}{2J+1}$ and $|\Psi_{nJM}(\phi;t)\rangle = U(\phi;t,0)|nJM\rangle$, where U is the time-evolution operator for the total system and $|nJM\rangle$ the field-free initial state, with J denoting the total angular momentum of the system, M the corresponding magnetic quantum number, and n the remaining quantum numbers. We note, in passing, that the Hamiltonian and hence the time-evolution operator have a parametric dependence on ϕ through the interaction with the external field. We evaluate the ensemble average Eq. (4) by using the position-eigenstate basis and thereby obtain

$$\left[\frac{\partial^3 P}{\partial q_x \partial q_y \partial q_z}(\vec{q},\phi)\right] = \frac{1}{2J+1}\sum_{M=-J}^{J}\left|\int d\vec{r}(\Psi_{\vec{q}}^-)^*\Psi_{nJM}(\phi;t)\right|^2. \tag{6}$$

By using the relation [40]

$$\int d\Omega D_{M'M}^{(J)}(\alpha,\beta,\gamma)D_{M''M}^{(J)*}(\alpha,\beta,\gamma) = \frac{8\pi^2}{2J+1}\delta_{M'M''}, \tag{7}$$

where $D_{M'M}^{(J)}(\alpha,\beta,\gamma)$ are the Wigner rotation functions, (α,β,γ) the Euler angles, and $d\Omega = \sin(\beta)d\beta d\alpha d\gamma$, Eq. (6) can also be expressed as

$$\left[\frac{\partial^3 P}{\partial q_x \partial q_y \partial q_z}(\vec{q},\phi)\right] = \frac{1}{8\pi^2}\int d\Omega\left|\int d\vec{r}(\Psi_{\vec{q}}^-)^*\Psi_{nJM'}(\Omega,\phi;t)\right|^2. \tag{8}$$

Here $\Psi_{nJM'}(\Omega,\phi;t)$ is a solution to the TDSE corresponding to the rotated initial state $D(\Omega)|nJM'\rangle$, with D the rotation operator and $\Omega = (\alpha,\beta,\gamma)$. However, $\Psi_{nJM'}(\Omega,\phi;t) = \exp(-i\hat{J}_z\phi)\Psi_{nJM'}(\Omega',\phi = 0;t)$ with $\Omega' = (\alpha - \phi,\beta,\gamma)$ [36]. Thus

$$\left[\frac{\partial^3 P}{\partial q_x \partial q_y \partial q_z}(\vec{q},\phi)\right] = \frac{1}{8\pi^2}\int d\Omega\left|\int d\vec{r}\ (\Psi_{\vec{q}}^-)^*\exp(-i\hat{J}_z\phi) \times \Psi_{nJM'}(\Omega',\phi = 0;t)\right|^2. \tag{9}$$

The rotation of a scattering wave function with asymptotic momentum $\vec{q}$ can be accomplished just by rotating the asymptotic momentum [i.e., $\exp(i\hat{J}_z\phi)\Psi_{\vec{q}}^- = \Psi_{\vec{q}'}^-$, where $\vec{q}' = \mathbf{R}_z(-\phi)\vec{q}$, with $\mathbf{R}_z$ the 3×3 orthogonal matrix that generates counterclockwise rotations around the z axis] [40]. This means that

$$\left[\frac{\partial^3 P}{\partial q_x \partial q_y \partial q_z}(\vec{q},\phi)\right] = \frac{1}{8\pi^2}\int_0^{2\pi}\int_0^{2\pi}\int_0^{\pi}\sin(\beta)d\beta d\alpha d\gamma \times\left|\int d\vec{r}\ (\Psi_{\vec{q}'}^-)^*\Psi_{nJM'}(\Omega',\phi = 0;t)\right|^2. \tag{10}$$

Finally this expression can be rewritten as

$$\begin{aligned}\left[\frac{\partial^3 P}{\partial q_x \partial q_y \partial q_z}(\vec{q},\phi)\right] &= \frac{1}{8\pi^2}\int_0^{2\pi}\int_{-\phi}^{2\pi-\phi}\int_0^{\pi}\sin(\beta)d\beta d\alpha d\gamma \\ &\quad\times\left|\int d\vec{r}\ (\Psi_{\vec{q}'}^-)^*\Psi_{nJM'}(\Omega,\phi = 0;t)\right|^2 \\ &= \left(\frac{\partial^3 P}{\partial q_x \partial q_y \partial q_z}(\vec{q}',\phi = 0)\right),\end{aligned} \tag{11}$$

owing to the uniformity of the distribution function over the orientations, $G(\Omega) = 1/(8\pi^2)$. Thus a change in the CEP from $\phi = 0$ to $\phi = \phi'$ corresponds to a rotation of the system around the z axis by ϕ'. This is illustrated in Fig. 7, which shows the ensemble average of the exact momentum distribution in the xy polarization plane for Ar atoms initially in an incoherent mixture of $3p_x$ or $3p_y$ states for two different values of the CEP, $\phi = -\pi/2$ and $\phi = 0$. Notice that the validity of Eq. (11) does not require the SAE or the dipole approximation, which can easily be checked by going through the steps leading to Eq. (11) and maintaining full retardation and accounting for all electrons.

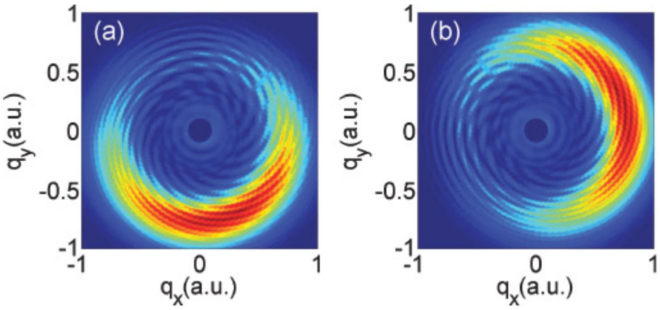

FIG. 7. (Color online) Ensemble average of the SAE, TDSE momentum distributions in the xy polarization plane for argon initially in a uniform incoherent mixture of $3p_x$ and $3p_y$ states. The laser parameters are as follows: angular frequency $\omega = 0.057$, corresponding to 800 nm, peak intensity $I = 1.06 \times 10^{14}$ W/cm^2, carrier-envelope phase (a) $\phi = -\pi/2$, (b) $\phi = 0$, and number of optical cycles $N = 3$.

The pure $3p_x$ and $3p_y$ states of Ar, of course, do not fulfill the requirements for the validity of Eq. (11) and hence the CEP effects observed in this paper are not in general simple rotations. It is, nevertheless, still possible to express momentum distributions for $3p_x$ in terms of momentum distributions for $3p_y$. Symmetry considerations immediately lead to the following formula:

$$\frac{\partial^3 P_{3p_y}}{\partial q_x \partial q_y \partial q_z}(\phi + \pi/2) = \mathbf{R}_z(\pi/2)\frac{\partial^3 P_{3p_x}}{\partial q_x \partial q_y \partial q_z}(\phi), \quad (12)$$

where ϕ is the CEP. This geometric correspondence is illustrated in Figs. 1 and 2, where we note that $\partial^3 P_{3p_y}/(\partial q_x \partial q_y \partial q_z)(\phi = 0) = \mathbf{R}_z(\pi/2)\partial^3 P_{3p_x}/(\partial q_x \partial q_y \partial q_z)$ $(\phi = -\pi/2)$.

IV. CONCLUSION

We have investigated strong-field ionization of Ar($3p_x$) and Ar($3p_y$) in the presence of a strong circularly polarized laser pulse by calculating the photoelectron momentum distribution using the TDSE. These systems model the ionization from an oriented target with a single angular nodal plane interacting with a circularly polarized laser pulse, a scenario that could be realized in an oriented molecular target. Our results are compared with results obtained using the LG-SFA and, up to a relatively small rotation of the distribution that is well understood as a combined field and potential effect [14], good agreement is observed, emphasizing the LG-SFA as a valuable tool for studying ionization by circularly polarized pulses. More importantly, both TDSE and LG-SFA results show distinct signatures of the initial states as well as the temporal shape of the applied pulse, which indicate that strong-field ionization by circularly polarized pulses may serve as a probe for revealing nodal structure and also changes that may occur during chemical reactions. This assertion is strengthened by strong-field calculations that involve orbitals with different angular symmetry including aligned benzene.

ACKNOWLEDGMENTS

This work was supported by the Danish Research Agency (Grant No. 2117-05-0081).

[1] A. Scrinzi, M. Y. Ivanov, R. Kienberger, and D. M. Villeneuve, J. Phys. B **39**, R1 (2006).

[2] F. Krausz and M. Ivanov, Rev. Mod. Phys. **81**, 163 (2009).

[3] H. Stapelfeldt and T. Seideman, Rev. Mod. Phys. **75**, 543 (2003).

[4] R. Baumfalk, N. H. Nahler, and U. Buck, J. Chem. Phys. **114**, 4755 (2001).

[5] H. Sakai, S. Minemoto, H. Nanjo, H. Tanji, and T. Suzuki, Phys. Rev. Lett. **90**, 083001 (2003).

[6] H. Tanji, S. Minemoto, and H. Sakai, Phys. Rev. A **72**, 063401 (2005).

[7] U. Buck and M. Farnik, Int. Rev. Phys. Chem. **25**, 583 (2006).

[8] L. Holmegaard, J. H. Nielsen, I. Nevo, H. Stapelfeldt, F. Filsinger, J. Küpper, and G. Meijer, Phys. Rev. Lett. **102**, 023001 (2009).

[9] I. Nevo, L. Holmegaard, J. H. Nielsen, J. L. Hansen, H. Stapelfeldt, F. Filsinger, G. Meijer, and J. Küpper, Phys. Chem. Chem. Phys. **11**, 9912 (2009).

[10] P. Eckle, M. Smolarski, P. Schlup, J. Biegert, A. Staudte, M. Schöffler, H. G. Muller, R. Dörner, and U. Keller, Nat. Phys. **4**, 565 (2008).

[11] P. Eckle, A. N. Pfeiffer, C. Cirelli, A. Staudte, R. Dörner, H. G. Muller, M. Büttiker, and U. Keller, Science **322**, 1525 (2008).

[12] A. Staudte *et al.*, Phys. Rev. Lett. **102**, 033004 (2009).

[13] M. Magrakvelidze, F. He, S. De, I. Bocharova, D. Ray, U. Thumm, and I. V. Litvinyuk, Phys. Rev. A **79**, 033408 (2009).

[14] C. P. J. Martiny, M. Abu-samha, and L. B. Madsen, J. Phys. B **42**, 161001 (2009).

[15] T. K. Kjeldsen, C. Z. Bisgaard, L. B. Madsen, and H. Stapelfeldt, Phys. Rev. A **68**, 063407 (2003).

[16] T. K. Kjeldsen, C. Z. Bisgaard, L. B. Madsen, and H. Stapelfeldt, Phys. Rev. A **71**, 013418 (2005).

[17] M. Busuladžić, A. Gazibegović-Busuladžić, and W. Becker, Phys. Rev. Lett. **100**, 203003 (2008).

[18] M. Meckel *et al.*, Science **320**, 1478 (2008).

[19] L. Holmegaard, J. L. Hansen, L. Kalhøj, S. L. Kragh, H. Stapelfeldt, F. Filsinger, J. Küpper, G. Meijer, D. Dimitrovski, M. Abu-samha, C. P. J. Martiny, and L. B. Madsen, Nature Phys. **6**, 428 (2010).

[20] L. V. Keldysh, J. Exp. Theor. Phys. **47**, 1945 (1964) [Sov. Phys. JETP **20**, 1307 (1965)].

[21] M. Lewenstein, P. Balcou, M. Y. Ivanov, A. L'Huillier, and P. B. Corkum, Phys. Rev. A **49**, 2117 (1994).

[22] T. K. Kjeldsen and L. B. Madsen, J. Phys. B **37**, 2033 (2004).

[23] P. B. Corkum, Phys. Rev. Lett. **71**, 1994 (1993).

[24] H. G. Muller and F. C. Kooiman, Phys. Rev. Lett. **81**, 1207 (1998).

[25] H. G. Muller, Laser Phys. **9**, 138 (1999).

[26] T. K. Kjeldsen, L. A. A. Nikolopoulos, and L. B. Madsen, Phys. Rev. A **75**, 063427 (2007).

[27] D. B. Milosěvić, G. G. Paulus, D. Bauer, and W. Becker, J. Phys. B **39**, R203 (2006).

[28] C. P. J. Martiny and L. B. Madsen, Phys. Rev. A **76**, 043416 (2007).

[29] C. P. J. Martiny and L. B. Madsen, Phys. Rev. A **78**, 043404 (2008).

[30] T. Morishita, Z. Chen, S. Watanabe, and C. D. Lin, Phys. Rev. A **75**, 023407 (2007).

[31] A. Rudenko, K. Zrost, C. D. Schröter, V. L. B. de Jesus, B. Feuerstein, R. Moshammer, and J. Ullrich, J. Phys. B **37**, L407 (2004).

[32] C. M. Maharjan, A. S. Alnasser, I. Litvinyuk, P. Ranitovic, and C. L. Cocke, J. Phys. B **39**, 1955 (2006).

[33] D. G. Arbó, K. I. Dimitriou, E. Persson, and J. Burgdörfer, Phys. Rev. A **78**, 013406 (2008).

[34] M. Abu-samha, D. Dimitrovski, and L. B. Madsen, J. Phys. B **41**, 245601 (2008).

[35] M. W. Schmidt *et al.*, J. Comput. Chem. **14**, 1347 (1993).

[36] C. P. J. Martiny and L. B. Madsen, Phys. Rev. Lett. **97**, 093001 (2006).

[37] V. Roudnev and B. D. Esry, Phys. Rev. Lett. **99**, 220406 (2007).

[38] J. J. Hua and B. D. Esry, J. Phys. B **42**, 085601 (2009).

[39] J. J. Sakurai, *Modern Quantum Mechanics* (Addison-Wesley Publishing Company, Inc., New York, 1994).

[40] R. N. Zare, *Angular Momentum* (John Wiley & Sons, Inc., New York, 1988).